

**ČESKÉ VYSOKÉ  
UČENÍ TECHNICKÉ  
V PRAZE**

**FAKULTA  
STROJNÍ**



**TEZE  
DISERTAČNÍ  
PRÁCE**



CZECH TECHNICAL UNIVERSITY IN PRAGUE  
FACULTY OF MECHANICAL ENGINEERING  
DEPARTMENT OF MECHANICS, BIOMECHANICS AND MECHATRONICS

Summary of Dissertation

Numerical Implementation  
of Distortional Hardening Models

Ing. René Marek

*Supervisor:* Ing. Jiří Plešek, CSc.

*Doctoral Study Programme:* Mechanical Engineering

*Study Field:* Mechanics of Solids, Deformable Bodies and Continua

Dissertation thesis statement for obtaining the academic title  
of “Doctor” abbreviated to “Ph.D.”

Prague

January 2018

Title in the Czech language: Numerická implementace modelů se směrovým  
deformačním zpevněním

This doctoral thesis is an outcome of a full-time doctoral study programme at the Department of Mechanics, Biomechanics and Mechatronics, Faculty of Mechanical Engineering, Czech Technical University in Prague.

Disertant: Ing. René Marek  
Department of Mechanics, Biomechanics and Mechatronics  
Faculty of Mechanical Engineering  
Czech Technical University in Prague  
Technická 4, 166 07 Prague 6, Czech Republic

Supervisor: Ing. Jiří Plešek, CSc.  
Institute of Thermomechanics of the Czech Academy of Sciences,  
v.v.i.  
Dolejšková 1402/5, 182 00 Praha 8, Czech Republic

Reviewers: Assoc. Prof. Radim Halama, Ph.D.  
Prof. Ing. Jindřich Petruška, CSc.  
Assoc. Prof. Miroslav Španiel, CSc.

The thesis was set out on:

The defense of the dissertation thesis will take place on:

The thesis is available in the Department of Science and Research of Faculty of Mechanical Engineering, CTU in Prague, Technická 4, Praha 6 – Dejvice.

Prof. Ing. Michael Valášek, DrSc.  
Head of Doctoral Study Field Mechanical Engineering  
Faculty of Mechanical Engineering CTU in Prague

## **Annotation**

The presented thesis describes the formulation of two new constitutive models of metal plasticity within the realm of small strains, both featuring directional distortional hardening. New yield functions have been proposed with distortion and cross-effect control. The models feature new kinematic hardening rule that builds on the premise of multisurface plasticity while keeping the amount of internal variables low. The models' intended use is the study of multiaxial ratcheting—the cumulation of plastic deformation in combined loading, and ways of its calibration. Their possible real application lies in cyclic multiaxial operational loading present in pressurized piping systems and in some very specific applications. The models have been implemented into a UMAT subroutine for FE-system Abaqus.

## **Anotace**

Předložená práce popisuje formulaci dvou nových konstitutivních modelů plasticity se směrovým zpevněním pro oblast malých deformací. Pro modely byly navrženy nové funkce plasticity s řízením distorze a příčného rozměru. Modely mají zcela nový zákon kinematického zpevnění, který vychází z principu mnohaplochové plasticity, avšak zachovává malé množství vnitřních proměnných. Zamýšleným použitím modelů je studie víceosé kumulativní deformace a způsoby kalibrace. Jejich možné praktické uplatnění spočívá v cyklickém víceosém provozním zatížení v tlakových potrubních systémech a v některých velmi specifických aplikacích. Modely byly implementovány ve formě subroutine UMAT pro MKP-systém Abaqus.

# Contents

<b>1</b>	<b>Current Status of Research</b>	<b>1</b>
1.1	Notable models with advanced hardening . . . . .	3
1.2	Models with distortional hardening . . . . .	4
<b>2</b>	<b>Goals of Dissertation</b>	<b>6</b>
<b>3</b>	<b>Methods</b>	<b>7</b>
3.1	Finite element method . . . . .	7
<b>4</b>	<b>Results</b>	<b>11</b>
4.1	New coupled bounding surface model . . . . .	11
4.2	Numerical tests . . . . .	22
<b>5</b>	<b>Conclusion</b>	<b>25</b>
5.1	Future ways of distortion generation . . . . .	26

## Chapter 1

# Current Status of Research

Refinement of constitutive plasticity models is a continuing trend. Its aim is to increase accuracy and credibility of their predictions. This brings a higher chance of success when optimizing the distribution of operational stresses for the purpose of lowering fatigue, increasing safety or guaranteeing proper function by predicting deformation during operation.

After a successful attempt to simulate the hardening curve of material by the use of kinematic and isotropic hardening, applicable even for complex uniaxial cyclic loadings, the scientific community started to focus on multiaxial loading sequences and a possible influence of directional distortional hardening, which addresses distortion of the elastic region in the stress space.

The ongoing research into multiaxial ratcheting simulation only recently explored the use of such models. A great number of authors utilized a large set of experiments assembled in [7],[6] and [1]. However, these and other published experiments do not explore the shape of the distortion. The use of distorted hardening models on these data, such as [4] or [16], lacks an important piece of the information needed to adapt the kinematic rules and follow the real position of the yield surface. Better results are achieved in [5], having both types of experiments available. Such research is an iterative process of simulation, to proposition of experiments, to improvement of simulations. The experimental campaign needs to be interconnected with the modeling team and can hardly be assigned to a third party.

Fortunately, experimental facilities are becoming available to us on several institutions in Czech Republic, USA and Taiwan. Experimental measurement

to such detail necessary for these models is very complex and often employs dynamic control of the machine displacement according to real-time data analysis. To successfully prepare a trajectory for the experiment, a reliable simulation is consulted. Increased precision of measurement is reachable in such trajectories, where the material's response is most pronounced, e.g. attacking the yield threshold perpendicularly. Therefore, a powerful model is needed as a basis for the design of experiments and for validation of new features and evolution rules. Recently, new ideas came to mind, how to speedup calibration using just one or two specimens. A complex loading pattern could target specific parameters of the model to get the best initial calibration before numerical refinement is performed.

This thesis focuses on modeling in small deformations, where the application of such models is more sensible. Although the distortion of the elastic region is clearly measurable, its influence on the behavior of structures is generally minimal. In proportional loading in stress space, distortion of the elastic region is rotationally symmetrical about the loading direction and is manifested by an increase in the curvature of the frontal apex and flattening of the rear. To expose this phenomenon, multiaxial cyclic behavior has to be studied. In real application, that includes the operation of pressure systems and pipelines, where pressure and temperature loads combine. Other uses may include circularity violation, also called ovalization, of large diameter pipes from various loadings at seabed, mounting of heavy machinery during earthquake and other limit loadings, coiled springs, etc.

In this thesis, two new constitutive models are suggested, the first being the stepping stone for the second one. Sufficient convexity conditions of the yield surface have been derived for both models. Both models have been implemented in Abaqus and subjected to a multitude of tests concerning numerical error and various in-depth phenomena.

Although these models may find their practical application in their presented form, it is not intended. The theory of multiaxial ratcheting is still young. A very large set of data has to be obtained experimentally for such a model to be finalized and to give reliable predictions. To initiate an experimental campaign consisting of up to a hundred specimens is a strategic decision for the near future.

## 1.1 Notable models with advanced hardening

A thorough analysis of uniaxial and multiaxial ratcheting on internally pressurized specimens made of mild steel has been presented by Corona, Hassan and Kyriakides in [7, 6] and [1]. Various kinematic hardening rules were employed focusing on simpler schemes to see whether any of them could be used for large-scale simulations. Greatest differences in predictions were met when combining different types of tests on single calibration. Varying the amplitudes and internal pressure for the same type of test had a much lesser impact.

As a basis for a reliable universal model, excellent uniaxial ratcheting predictions need to be achieved. A strong contender is the SANISTEEL model in [10] using the Bounding Surface framework. An initially fixed non-hardening BS induces a perfectly plastic response (plateau), while the kinematic and isotropic parts evolve. This can be demonstrated by unloading—the material will yield before nominal yield strength in opposite direction is reached. The yield surface moves within the Bounding Surface. After depleting the plateau threshold, the Bounding Surface is unlocked and its movement now allows slow reach of higher levels of stress. The authors studied three simple rules for Bounding Surface kinematic hardening, differing in the way the BS moves when reloading and whether it has any asymptotic limits of position. These rules have different effects on ratcheting speed. Ultimately, the decision for a particular rule, or a proposal of a new one, will be made after observing a greater amount of experimental data. The choice of such kinematic rule for the intended model is completely free, having no effect on the yield function and its derivatives. Limits have to be kept for the position of the Bounding Surface, as it rapidly increases the amount of storable plastic free energy.

A multisurface kinematic hardening rule offers even better predictions for complex loading trajectories, as it imitates our understanding of the inner workings of the material. Each surface represents a subset of slip systems, whose activation require a particular state of stress. An interesting observation were made by Zhang, Benítez and Montáns in [22]. A reproduction of yield surface tracing procedure on a model featuring multisurface kinematic rule with smooth elastic-plastic transition showed a noticeable conformity with experimental data.

A deep study of equi-strain maps on distorted and non-distorted models will ultimately answer, whether the concept of distorted yield surface is a right way to proceed, or whether just the distortion of kinematic rule, planned or induced, is more logical. A yield surface with very precisely defined yield threshold loses the notion of shape, as the plastic modulus approaches infinity.

## 1.2 Models with distortional hardening

A number of different ways have been described throughout the literature on how to distort the shape of the yield function. The straight-forward approach presented in [12] is to vary the radius of the von Mises hypersphere. In this case, it is done by a series of harmonic functions according to the position angle  $\arccos(\mathbf{n}_r : \mathbf{n}_z)$ , where  $\mathbf{n}_z$  is the unit-norm director tensor defining the orientation of the distortion and  $\mathbf{n}_r$  is the unit-norm tensor along the "radial" tensor  $(\mathbf{s} - \boldsymbol{\alpha})$ . Its definition will therefore be

$$\mathbf{n}_r \equiv \frac{\mathbf{s} - \boldsymbol{\alpha}}{\|\mathbf{s} - \boldsymbol{\alpha}\|}, \quad (1.1)$$

where the tensor norm is defined as

$$\|\mathbf{x}\| \equiv \sqrt{\mathbf{x} : \mathbf{x}} = \sqrt{x_{ij}x_{ij}}. \quad (1.2)$$

In the original work,  $\mathbf{n}_z$  is the unit-norm tensor simply in the direction of back-stress.

Two or more harmonic components are needed, as the desired function for fully formed distortion is quite complex. Adjustment for cross effect is non-trivial and a high price for trigonometric computations does not make this a good choice.

Extensive study by Kurtyka and Źyczkowski in [8],[9] demonstrated remarkable agreement of their model with experimental data. Distortion was modeled by geometrical description in Ilyushin's auxiliary stress space. Intact proportional characteristics, explicit independent control of the transverse dimension

(the cross effect), independent orientation of the elastic region, and a possibility of non-symmetric distortion are its most valuable features. This yield surface could be used as a basis for a new model. However, the handling of the yield function is difficult and the possibility of non-symmetric distortion does not really offer the capabilities needed.

A very promising approach by Shutov and Ihleman in [17] and [18] is represented by a rotationally symmetrical yield surface generated by a meridian assembled from arc sections. For intermediate distortion, a weighted average between initial von Mises hypersphere and a fully distorted shape was chosen. This model has a very simple gradient equation. If the intermediate shape were also described by arc sections, the yield function would have had a single step solution for radial corrector method, as well as for the plastic part detection of the trial stress. In other models, both processes require multiple calculations of the yield function and its gradient. However, calculation of the arc section positions for different intensity of distortion as well as cross effect would be quite difficult. By its definition, there are no possible expansions towards non-symmetrical distortion.

## Chapter 2

# Goals of Dissertation

1. Assembling a new model featuring directional distortional hardening.
  - (a) Proposal of a new yield function with controlled transverse size.
  - (b) Derivation of convexity condition.
  - (c) Proposal of kinematic laws and bounding surface interaction rules.
2. Implementation into a finite element code.
  - (a) Euler forward scheme. Assessment of other methods.
  - (b) Stability tests. Analysis of possibilities for optimization.
3. Numerical calibration on available ratcheting experiments.

## Chapter 3

# Methods

### 3.1 Finite element method

Following [A1], the basic laws of computational plasticity within the Finite Element method will be reminded. The equilibrium equation discretized by the Finite Element method reads

$$\int_{\Omega} \mathbf{B}^T \boldsymbol{\sigma} d\Omega = \mathbf{R}, \quad (3.1)$$

where  $\mathbf{B}$  is the strain-displacement matrix,  $\boldsymbol{\sigma}$  is the stress column vector and  $\mathbf{R}$  is the equivalent external force acting on the nodal points. As the material behaves elasto-plastically, the stress-strain relation is no longer linear but forms an algebro-differential system according to the hardening laws. In general, this system can only be solved numerically.

#### 3.1.1 Incremental problem

The nonlinear equations of elastoplasticity on the level of governing relations between nodal displacements and forces are solved by a suitable iteration procedure. Starting at time  $t$  in an equilibrium state of stress  ${}^t\boldsymbol{\sigma}$ , plastic strain  ${}^t\boldsymbol{\epsilon}_p$ , and with a set of tensor and scalar internal variables  $\{{}^t\mathbf{x}_i, {}^t y_j\}$ , one is to determine  ${}^{t+1}\boldsymbol{\sigma}$ ,  ${}^{t+1}\boldsymbol{\epsilon}_p$  and  $\{{}^{t+1}\mathbf{x}_i, {}^{t+1}y_j\}$  at time  $t+1$ . For this purpose, the iteration procedure proposes trial increment  $\Delta\boldsymbol{\epsilon}^{\text{trial}}$ , which is imported into the constitutive model to calculate stress response, so that a new improved estimation of  $\Delta\boldsymbol{\epsilon}^{\text{trial}}$

can be obtained. This process is repeated until equilibrium is reached. The quasi-Newton Broyden-Fletcher-Goldfarb-Shano (BFGS) method may be employed to this end, as introduced in [11].

### 3.1.2 Integration scheme

There are a number of integration schemes suitable for general plastic constitutive model. Due to unconditional stability, the implicit backward Euler scheme

$${}^{t+1}\boldsymbol{\sigma} = {}^t\boldsymbol{\sigma} + \Delta\boldsymbol{\sigma}^{\text{trial}} - \Delta\lambda\mathbf{C} \left. \frac{\partial f}{\partial \boldsymbol{\sigma}} \right|_{t+1}, \quad (3.2)$$

is preferred. The main downside is the computational demands, as it has to be iterated. Additionally, within Eq. (3.2) the value of plastic multiplier has to be solved, so for the updated stress remains  $f(\boldsymbol{\sigma}, \mathbf{x}_i, y_j)|_{t+1} = 0$ .

In this thesis, many abrupt changes in the developed model happen during general loading, such as unlocking the plateau, or complex internal processes withing the new kinematic rule. Despite good experience with the substepping method by Sloan in [19], as it was successfully implemented to a distortional model in [A3], a slight modification of explicit scheme is used, which enables greater control over the integration step length and therefore interrupts the integration process in the moments of discrete changes of internal variables. The stress response is calculated by the tangent stiffness-radial corrector method, originally introduced in [21]. After proposing a trial stress value from Hooke's law

$$\boldsymbol{\sigma}^{\text{trial}} = {}^t\boldsymbol{\sigma} + \Delta\boldsymbol{\sigma}^{\text{trial}} = {}^t\boldsymbol{\sigma} + \mathbf{C}\Delta\boldsymbol{\epsilon}^{\text{trial}}, \quad (3.3)$$

the elastic check is performed. If  $f(\boldsymbol{\sigma}^{\text{trial}}) < \text{tol}$ , the elastic law is considered valid and the stress response is set as  ${}^{t+1}\boldsymbol{\sigma} = \boldsymbol{\sigma}^{\text{trial}}$ . Otherwise, if the elastic check is not fulfilled, a search for the actual yield stress is initiated. The intersection point

$$\boldsymbol{\sigma} = {}^t\boldsymbol{\sigma} + (1 - g)\Delta\boldsymbol{\sigma}^{\text{trial}} \quad \text{for } g \in [0, 1] \quad (3.4)$$

with the yield surface  $f(\boldsymbol{\sigma}, \mathbf{x}_i, y_j)|_t = 0$  is computed iteratively by Newton's method, i.e.

$$g_{i+1} = g_i + \frac{f}{\frac{\partial f}{\partial \boldsymbol{\sigma}} : \Delta \boldsymbol{\sigma}^{\text{trial}}} \Bigg|_{\boldsymbol{\sigma} = {}^t \boldsymbol{\sigma} + (1-g_i) \Delta \boldsymbol{\sigma}^{\text{trial}}} \quad (3.5)$$

until the prescribed tolerance is met. The remaining plastic part  $\Delta \boldsymbol{\sigma}_p^{\text{trial}} = g \Delta \boldsymbol{\sigma}^{\text{trial}}$  of the trial stress enters the procedure described in the next section, from which a new equilibrium state  ${}^{t+1} \boldsymbol{\sigma}$ ,  ${}^{t+1} \boldsymbol{\epsilon}_p$ ,  $\{ {}^{t+1} \mathbf{x}_i, {}^{t+1} y_j \}$ , satisfying the plasticity condition, arises. More information is available in [15] together with the proof of convergence for an arbitrary convex yield function. This state returns to the core of the implicit finite element solver as a basis for a new iteration of the trial estimation.

A square root form of the proposed yield function does not represent a hyperconical function. Still, for the proportional loading only, the function on the main axis is linear and so the above iteration process converges to  $f = 0$  within one step. An osculation sphere on the frontal apex and on the rear may speedup these calculations on some specific loading conditions.

Handling all the rates as increments in dimensionless time, one may convert the plastic multiplier into the incremental form as

$$\Delta \lambda = \frac{\frac{\partial f}{\partial \boldsymbol{\sigma}} : \Delta \boldsymbol{\sigma}_p^{\text{trial}}}{K_p + \frac{\partial f}{\partial \boldsymbol{\sigma}} : \mathbf{C} \frac{\partial f}{\partial \boldsymbol{\sigma}}}. \quad (3.6)$$

Acquiring the plastic multiplier, the evolution rules can be followed to calculate  $\{ {}^{t+1} \mathbf{x}_i, {}^{t+1} y_j \}$ . Consequently, rewriting the differential form of the stress response into the incremental form, the stress tensor yields

$${}^{t+\Delta t} \boldsymbol{\sigma}^* = {}^t \boldsymbol{\sigma} + \Delta \boldsymbol{\sigma}^{\text{trial}} - \Delta \lambda \mathbf{C} \frac{\partial f}{\partial \boldsymbol{\sigma}} \Bigg|_t. \quad (3.7)$$

This updated value, marked by asterisk, generally does not satisfy the yield condition. A corrector scheme described below needs to be applied to achieve unconditional stability, see [13]. From this, the new value of stress  ${}^{t+\Delta t}\boldsymbol{\sigma}$  is obtained. To keep track of the accumulated plastic strain, the associative flow rule in scalar form may be used as

$$\Delta\epsilon_p = \sqrt{\frac{2}{3}}\Delta\lambda \left\| \frac{\partial f}{\partial \boldsymbol{\sigma}} \right\|. \quad (3.8)$$

### 3.1.3 Radial return corrector

Distortion of the yield surface offers various approaches to project the stress back onto the yield surface. A gradient method

$${}^{t+\Delta t}\boldsymbol{\sigma}_{i+1}^* = {}^{t+\Delta t}\boldsymbol{\sigma}_i^* - \frac{\partial f_i}{\partial \boldsymbol{\sigma}} f_i \left\| \frac{\partial f_i}{\partial \boldsymbol{\sigma}} \right\|^{-2} \quad (3.9)$$

may be the only choice when no convenient procedure exists. Again, for regions very close to the axis of the yield surface, analytical solution for projection on oscillation spheres may be used. It depends on the complexity of the terms defining their position and radius.

The radial return procedure will on many occasions require correction of the stress response from within the elastic region of the updated yield function. A step size limit has to be determined, so as to prevent this correction to be initiated from a position too close to the singularity at  ${}^{t+1}\boldsymbol{\alpha}$ , where it would lose clear definition of the appropriate projection point.

## Chapter 4

# Results

I suggested two new models with partially differing yield definitions. Both arise straight from the original Alpha model in [3]. The problem of elongation, that greatly limited the amount of materials suitable for the anticipated behavior, becomes truly visible when performing calibration procedure in [A2]. Answering this and several other problems that were encountered during development, these new yield functions are equipped with correcting affine transformations shortening their axial length and widening their crosswise diameter. Their kinematic rules have been completely rewritten. By adopting the Bounding Surface principle, the models are now capable of simulating an initial plateau, as well as a better elastic-plastic transition and ratcheting behavior. The first model features coupled distortion with kinematic law, maintaining its axis of the elastic region coincident with the origin of its Bounding Surface. The second model is an extension of the first one by means of uncoupling this bond.

### 4.1 New coupled bounding surface model

Using a square root form of the original Alpha model yield condition and using correcting transformations on the radial tensor, the yield condition of the new model acquires the following form:

$$f(\boldsymbol{\sigma}) = \sqrt{\frac{3}{2} [1 - c \|\mathbf{z}\| (\mathbf{n}_r : \mathbf{z})]} \|\mathbf{b}\| - k = 0, \quad (4.1)$$

where  $c$  remains as the distortional parameter,  $\mathbf{z}$  serves as a definition of the main axis of the Yield Surface and the aforementioned transformations are covered in the transformed radial stress  $\mathbf{b}$ . The size of the Yield Surface is controlled by the evolving isotropic parameter  $k$ . In this particular model, tensor  $\mathbf{z}$  acquires the form

$$\mathbf{z} = \boldsymbol{\alpha} - \boldsymbol{\beta}, \quad (4.2)$$

where  $\boldsymbol{\alpha}$  and  $\boldsymbol{\beta}$  are the traditional backstress and the center of the Bounding Surface, respectively. In effect, the main axis of the YS always aims from  $\boldsymbol{\beta}$ , which makes the interaction between YS and BS very simple.

To simplify calibration, the frontal apex always stays the same distance from backstress. When distortion occurs, the apex increases curvature, while the rear flattens and draws closer to the value of backstress. The actual intensity of the distortion is proportional to the norm of  $\mathbf{z}$ . This implies a series of problems. Due to the nonlinear nature of the forming of distortion, a pronounced shape is present only when  $\|\mathbf{z}\|$  starts to saturate to its limit. Additionally, when unloading occurs, the flattening of the rear disappears back to the von Mises sphere where it remains in a constant distance from backstress. This implies a first order discontinuity in the stress response. To combat this phenomenon, an additional term  $\|\mathbf{z}\|$  has been added in the yield condition (4.1), smoothing out the onset of the generated distortion. This further delayed the appearance of a pronounced distortion. Therefore, the distortion had to be sped up. Using an internal function to do that was expected to unnecessarily complicate the yield condition and its gradients. Therefore, the distortion is rather kept constant once it reaches a chosen limit. The yield condition is therefore reformulated as follows:

$$f(\boldsymbol{\sigma}) = \sqrt{\frac{3}{2} [1 - c_{zz} (\mathbf{n}_r : \mathbf{n}_z)]} \|\mathbf{b}\| - k = 0, \quad (4.3)$$

where

$$c_{zz} = \min \{c\mathbf{z} : \mathbf{z}, c_{zz}^{\max}\}; \quad c_{zz}^{\max} \leq c_{\text{lim}}^1 \leq c_{\text{lim}}^0 \quad (4.4)$$

unifies the yield condition for semi- and fully distorted state. A necessary condition forming the limit  $c_{\text{lim}}^1$  stems from a convexity requirement derived later.

### 4.1.1 Contraction and cross effect

The modified radial stress  $\mathbf{b}$  consists of the original radial stress followed by an axial contraction reached by inverting the Yield function, so that the elongation of the frontal apex is exactly counteracted. This brings a potential for a much simpler analytical solution of monotonic loading. At the very least, a calibration of the model based on monotonic loading is not dependent on the distortional parameter  $c$ .

The modification of the transverse part follows for the full cross-effect control. Unexpectedly, it is done only half way. Not applying transformation to the unit tensor  $\mathbf{n}_r$  in the yield condition offers a larger diversity of shapes. If it were the case of full application, the shape would be precisely scaled in transverse direction and would be lacking in front apex curvature. The structure of  $\mathbf{b}$  for the nominal yield function (4.1) contains correction

$$\mathbf{b} = (1 - c_{cr} \|\mathbf{z}\|) (\mathbf{s} - \boldsymbol{\alpha}) + \left[ \frac{1}{\sqrt{1 - c\mathbf{z}:\mathbf{z}}} + c_{cr} \|\mathbf{z}\| - 1 \right] \mathbf{n}_z \mathbf{n}_z : (\mathbf{s} - \boldsymbol{\alpha}). \quad (4.5)$$

The new yield function is not conical any more, with negative implications for quick return mapping algorithms using central projection, as used in Eq. (29) in [A1].

The unification for limited distortion in Eq. (4.3) shapes Eq. (4.5) to the following form:

$$\mathbf{b} = (1 - c_{crz}) (\mathbf{s} - \boldsymbol{\alpha}) + \left[ \frac{1}{\sqrt{1 - c_{zz}}} + c_{crz} - 1 \right] \mathbf{n}_z \mathbf{n}_z : (\mathbf{s} - \boldsymbol{\alpha}), \quad (4.6)$$

where

$$c_{crz} = \min \{ c_{cr} \|\mathbf{z}\|, c_{crz}^{\max} \}. \quad (4.7)$$

For a homogenous polycrystalline metal without cavities, the associative flow rule is chosen as

$$\dot{\boldsymbol{\epsilon}}_p = \lambda \frac{\partial f}{\partial \boldsymbol{\sigma}}. \quad (4.8)$$

### 4.1.2 New kinematic hardening law

Due to the effect of distortion on the stress response during unloading, a new kinematic hardening rule had to be assembled. From the great many published kinematic rules that could be adopted, a new idea came to mind: A simplification of an otherwise well behaving multi-surface kinematic rule. This new approach rethinks the way the model remembers the history of loading, more specifically, it assumes that earlier history with less pronounced phenomena may be forgotten. In effect, this model uses a limited amount of tensors forming a hierarchy to represent distinct groups of nested yield surfaces of a multisurface equivalent, see Fig. 4.1. The backstress is simply a summation of individually evolved components as

$$\boldsymbol{\alpha} = \boldsymbol{\beta} + \sum_{i=1}^4 \boldsymbol{\alpha}_i \quad (4.9)$$

with the Bounding Surface center  $\boldsymbol{\beta}$  added to the sum, making the interactions within backstress kinematic rule relative to the BS, as it does seem to be its effect on the stress response.

When new direction of loading is introduced, the primary component of backstress now represents the newly formed band of the innermost equivalent surfaces. Smaller surfaces that are within the second band are continuously fed to the primary. During plastic loading, a flow of stress is present between the component tensors, while rapid transfers happen when new distinct direction of loading is introduced. In such a case, the history represented by the third component is irretrievably altered.

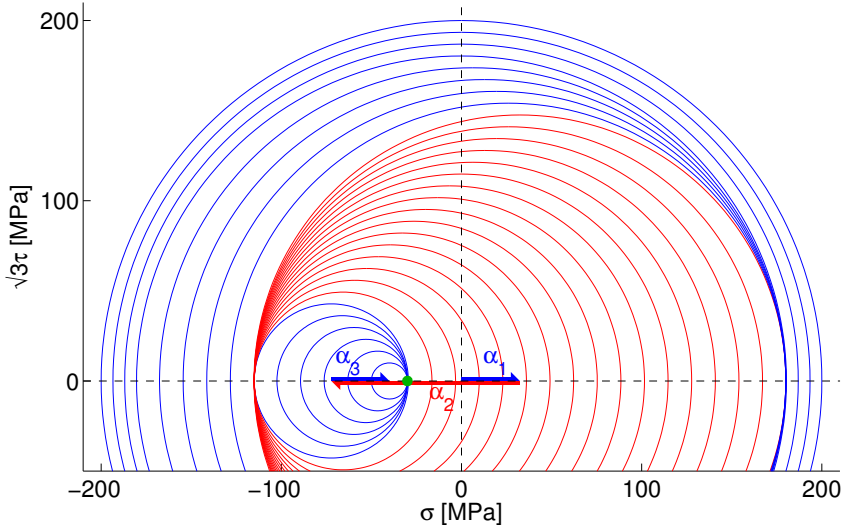


FIGURE 4.1: Backstress component tensors and their multi-surface equivalent for a virgin material after tension-compression-tension loading.

The multiaxial formulation of this model consists of the yield condition (4.3) with backstress confined in the Bounding Surface. The driving direction of the backstress kinematic rule uses its projection  $\alpha_B$  on the Bounding Surface. This is consistent with the formulation in [10]. The choice to use interaction on the level of backstress rather than stress comes from problems related to the distortion feature and its interaction with BS. However, the coupled distortion of this particular model does not have such problems, as it is always aiming outwards with its frontal apex. Still, it is chosen for it to limit the number of differences between coupled and uncoupled models. The definition of the driving tensor is as follows:

$$\mathbf{n}_{\alpha_B} \equiv \frac{\alpha_B - \alpha}{\|\alpha_B - \alpha\|}, \quad (4.10)$$

where the projection of the backstress on the Bounding Surface is in the direction of the outer normal tensor, as

$$\alpha^B \equiv \beta + \sqrt{\frac{2}{3}} K \mathbf{n}. \quad (4.11)$$

The situation is depicted in Figure 4.2, where blue is the Bounding Surface and green is the distorted Yield Surface.

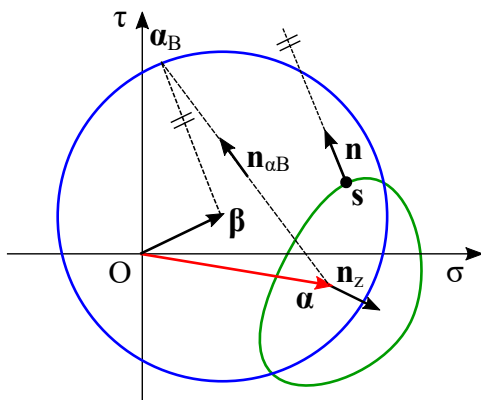


FIGURE 4.2: Definition of the backstress growing direction  $\mathbf{n}_{\alpha B}$

As the set of backstress components represent distinct bands of nested surfaces of a multisurface equivalent, a necessary transfer between the tensors is required. During loading, internal forces are stored by means of function

$$G_4 = \left( \sqrt{\frac{2}{3}} \bar{K} + h_1 \delta \right) \mathbf{n}_{\alpha B} \quad (4.12)$$

that represents opening of new slip systems for the storage of internal forces. A choice was made to apply this growth on the least active component, number 4.

The distance towards the projected backstress

$$\delta \equiv \|\alpha_B - \alpha\| \quad (4.13)$$

is used to shape and asymptotically limit the hardening curve when approaching the Bounding Surface. Once forces are stored, they can be very rapidly shared between components to simulate high values of plastic modulus during unloading. A dissipation function for such a process was contemplated, ultimately demonstrated to be unnecessary. The auxiliary components

$$\bar{\alpha}_2 = -F_2 \mathbf{n}_{\alpha 2} + p_s (\alpha_1 - \alpha_2) \quad (4.14)$$

$$\bar{\alpha}_3 = -F_3 \mathbf{n}_{\alpha 3} + p_s \alpha_2 \quad (4.15)$$

$$\bar{\alpha}_4 = G_4 \mathbf{n}_{\alpha B} - F_4 \mathbf{n}_{\alpha 4} \quad (4.16)$$

provide internal forces for the primary component

$$\bar{\alpha}_1 = (F_2 + F_3 + F_4) \mathbf{n}_{\alpha B} - p_s \alpha_1 \quad (4.17)$$

via the flow functions  $F_i$  acting in the directions represented by respective tensors  $\mathbf{n}_{\alpha i}$ .

Initiated by a significant change in the direction of loading, a new primary component may be introduced. This would be done by a cascade of transfers, as described later. Such a discrete change necessarily creates discontinuities of the stress response. For that reason, function  $p_s$  represents smoothing that is activated in the transient space between proportional loading and cases of rapid change in direction of loading, as

$$p_s = \langle \exp[-10 (\mathbf{n}_{\alpha B} : \mathbf{n}_{\alpha i} - 0.8)] - 1 \rangle. \quad (4.18)$$

For very distinct changes,  $p_s$  reaches virtual infinity and represents total transfer. The flow functions describe the rate in which the internal forces are shared among the components. An initial, memorized value of  $\delta$  was used in [10] to speedup the hardening response when short unloading occurs. The introduction

of such a distinct choice is problematic in relation to the continuity of the stress response, especially for multiaxial loading.

Within the structure of the backstress components, a value that serves a similar purpose can be found as

$$S_i = \sum_{j=1}^{i-1} \|\boldsymbol{\alpha}_j\|, \quad (4.19)$$

which represents the radius of the fictitious nested surface on the leading edge of the  $i$ -th band. With it, the flow function is assembled as follows:

$$F_i = h_2 h_{\text{dist}} \underbrace{\frac{\delta}{S_i + \varepsilon}}_{\text{Hardening}} \underbrace{\frac{1}{(S_i + \delta)^2 + \varepsilon}}_{\text{Speedup}} \left[ \underbrace{1 - \exp(-h_3 \|\boldsymbol{\alpha}_i\|)}_{\text{Depletion smoothing}} \right] F_{s_i}. \quad (4.20)$$

When using small yield surface, the return to previous level of stress after short unloading has to be that much quicker. So much in fact, that the Speedup function requires a quadratic term in the denominator.

### 4.1.3 Convexity condition

For a stable return mapping algorithm required by the Euler method used in this model, the convexity of the Yield function has to be ensured. The needed sufficient and necessary condition is for its Hessian matrix to be positive definite. By differentiating the gradient of the yield function

$$\frac{\partial \mathbf{f}}{\partial \boldsymbol{\sigma}} = \|\mathbf{b}\| \frac{c_{zz}}{\sqrt{\frac{8}{3} [1 - c_{zz} (\mathbf{n}_r : \mathbf{n}_z)]}} \frac{\mathbf{n}_r : \mathbf{n}_z \mathbf{n}_r - \mathbf{n}_z}{\|\mathbf{s} - \boldsymbol{\alpha}\|} + \sqrt{\frac{3}{2} [1 - c_{zz} (\mathbf{n}_r : \mathbf{n}_z)]} \frac{\mathbf{b}}{\|\mathbf{b}\|} : \frac{\partial \mathbf{b}}{\partial \boldsymbol{\sigma}}, \quad (4.21)$$

where

$$\frac{\partial \mathbf{b}}{\partial \boldsymbol{\sigma}} = (1 - c_{\text{crz}}) \mathbf{I}^D + \left( \frac{1}{\sqrt{1 - c_{zz}}} + c_{\text{crz}} - 1 \right) \mathbf{n}_z \otimes \mathbf{n}_z, \quad (4.22)$$

the Hessian matrix yields

$$\begin{aligned}
\frac{\partial^2 f}{\partial \boldsymbol{\sigma} \partial \boldsymbol{\sigma}} &= \frac{c \|\mathbf{z}\|}{\sqrt{\frac{8}{3} [1 - c \|\mathbf{z}\| (\mathbf{n}_r : \mathbf{z})]}} \frac{\mathbf{b}}{\|\mathbf{b}\|} : \frac{\partial \mathbf{b}}{\partial \boldsymbol{\sigma}} \otimes \frac{\mathbf{n}_r : \mathbf{z} \mathbf{n}_r - \mathbf{z}}{\|\mathbf{s} - \boldsymbol{\alpha}\|} + \\
&+ \sqrt{\frac{3}{32}} \frac{c^2 \|\mathbf{b}\| \|\mathbf{z}\|^2}{\sqrt{1 - c \|\mathbf{z}\| (\mathbf{n}_r : \mathbf{z})}^3} \frac{\mathbf{n}_r : \mathbf{z} \mathbf{n}_r - \mathbf{z}}{\|\mathbf{s} - \boldsymbol{\alpha}\|} \otimes \frac{\mathbf{z} - \mathbf{n}_r (\mathbf{n}_r : \mathbf{z})}{\|\mathbf{s} - \boldsymbol{\alpha}\|} + \\
&+ \frac{c \|\mathbf{z}\| \|\mathbf{b}\|}{\sqrt{\frac{8}{3} [1 - c \|\mathbf{z}\| (\mathbf{n}_r : \mathbf{z})]}} \cdot \frac{(\mathbf{I}^D - 3\mathbf{n}_r \otimes \mathbf{n}_r) (\mathbf{n}_r : \mathbf{z}) + \mathbf{z} \otimes \mathbf{n}_r + \mathbf{n}_r \otimes \mathbf{z}}{\|\mathbf{s} - \boldsymbol{\alpha}\|^2} + \\
&+ \left[ \frac{c \|\mathbf{z}\|}{\sqrt{\frac{8}{3} [1 - c \|\mathbf{z}\| (\mathbf{n}_r : \mathbf{z})]}} \frac{\mathbf{n}_r : \mathbf{z} \mathbf{n}_r - \mathbf{z}}{\|\mathbf{s} - \boldsymbol{\alpha}\|} \otimes \frac{\mathbf{b}}{\|\mathbf{b}\|} + \right. \\
&+ \left. \sqrt{\frac{3}{2} [1 - c \|\mathbf{z}\| (\mathbf{n}_r : \mathbf{z})]} \frac{\partial \mathbf{b}}{\partial \boldsymbol{\sigma}} : \frac{\mathbf{I} (\mathbf{b} : \mathbf{b}) - \mathbf{b} \otimes \mathbf{b}}{\|\mathbf{b}\|^3} \right] : \\
&: \left[ (1 - c_{cr} \|\mathbf{z}\|) \mathbf{I}^D + \left( \frac{1}{\sqrt{1 - c\mathbf{z} : \mathbf{z}}} + c_{cr} \|\mathbf{z}\| - 1 \right) \mathbf{n}_z \otimes \mathbf{n}_z \right], \quad (4.23)
\end{aligned}$$

where Eq. (4.22) is used.

Closely following the method in [14], the Hessian is required to fulfill the following condition:

$$\forall \boldsymbol{\phi} \neq \mathbf{0}: \quad \boldsymbol{\phi} : \mathbf{H} \boldsymbol{\phi} > 0, \quad (4.24)$$

where  $\boldsymbol{\phi}$  is an arbitrary second-order tensor. The structure of this condition enables normalizing  $|\boldsymbol{\phi}| = 1$  and further simplifying the numerical search. Using a number of substitutions, Eq. (4.24) reaches a fully scalar form as

$$\begin{aligned}
p\boldsymbol{\phi} : \mathbf{H} \boldsymbol{\phi} &= 2cL^2 x (1 - cL^2 x) (g^2 + 2ghx^2 + h^2 x^2) \cdot \\
&\cdot [g^2 (1 - y^2) + (h^2 + 2gh) (4xyz - 2z^2 + x^2 - 3x^2 y^2)] + \\
&+ 4g^2 (1 - cL^2 x)^2 [g^2 (1 - y^2) + h (h + 2g) (x^2 + z^2 - 2xyz)] - \\
&+ c^2 L^4 (g^2 + 2ghx^2 + h^2 x^2)^2 (xy - z)^2 \geq 0 \quad (4.25)
\end{aligned}$$

where  $g = (1 - Lc_{cr})$ ,  $h = \left[ \frac{1}{\sqrt{1 - L^2 |c|}} + Lc_{cr} - 1 \right]$ ,  $x = (\mathbf{n}_r : \mathbf{z})$ ,  $y = (\mathbf{n}_r : \boldsymbol{\phi})$  and  $z = (\mathbf{z} : \boldsymbol{\phi})$ . It is apparent from the Yield function (4.1, 4.5), that it is possible

to state  $\|\mathbf{z}\| \leftarrow L$ , as it is always multiplied by either  $c$ , or  $c_{cr}$ . Therefore  $L = \sqrt{\frac{2}{3}}(1/K_2 + 1/\kappa_4)$  as the limit size of the Bounding Surface. The solution for limit convexity would therefore be relative to the value of  $L$ . The always positive part  $p = 4\sqrt{\frac{2}{3}}\|\mathbf{s} - \boldsymbol{\alpha}\|\|g\mathbf{n}_r + h\mathbf{z}x\|^3(1 - cL^2x)^{3/2} \geq 0$  can be factored out.

Skipping a great deal of deriving and numerical solving, for the fused maximum distortion parameter, a sufficient condition holds

$$c_{zz}^{\max} = 0.968 \frac{-1 + \sqrt{1 + 16(1 - c_{cr0})^4}}{4(1 - c_{cr0})^2}. \quad (4.26)$$

#### 4.1.4 Model calibration

The model has been calibrated according to the experiment in [2].

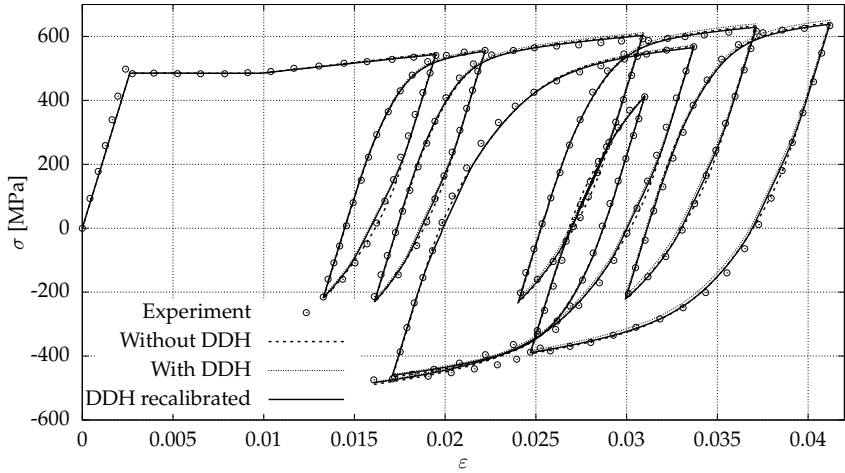


FIGURE 4.3: Demonstration of the model in random uniaxial cyclic loading calibrated to experimental data in [2].

Figure 4.4 depicts the same experiment with respect to the cumulative plastic strain. Initially,  $\alpha_4$  grows with the depletion of the plateau. First, a short unloading trajectory activates the first backstress segment.  $\alpha_4$  has stored forces in the opposite direction and is therefore eager to provide component  $\alpha_1$  with its content. After that, the original prestress returns and the primary component quickly gains forces from the secondary component.

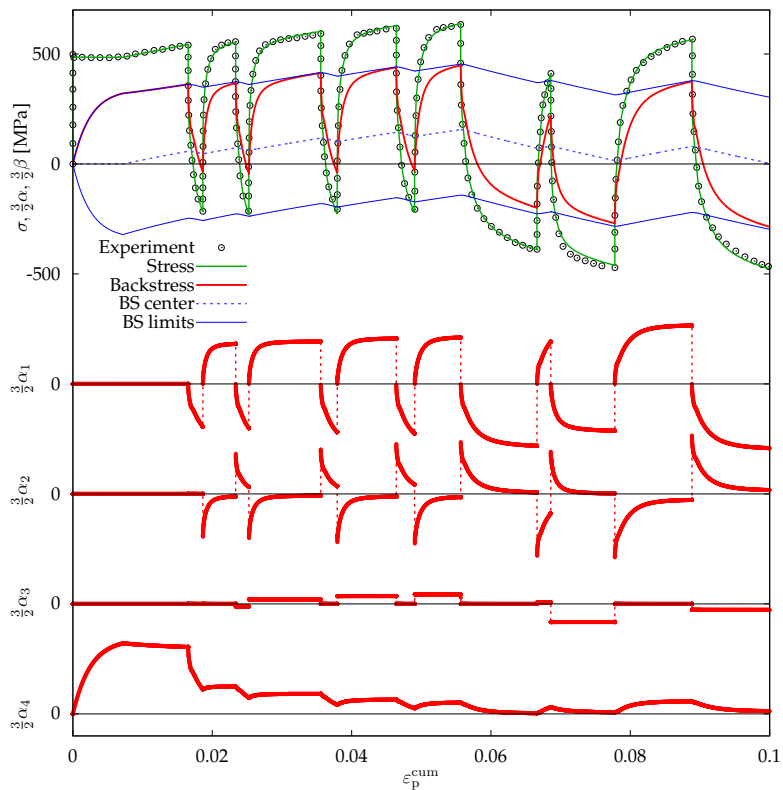


FIGURE 4.4: Backstress components during cyclic loading.

### 4.1.5 Integration step optimization

By principle, the Bounding Surface has to move much more slowly compared to the backstress. Therefore, it does not need to be checked for overshooting. The maximum plastic multiplier for the overall backstress kinematic rule is set with respect to the Bounding Surface as

$$\lambda_{\alpha} = \min \left\{ \frac{-\left(\bar{\mathbf{z}}:\mathbf{z} - \frac{2}{3}\bar{K}K\right) + \sqrt{D}}{3\left(\bar{\mathbf{z}}:\bar{\mathbf{z}} - \frac{2}{3}\bar{K}^2\right)}; \sqrt{\frac{2}{3}} \frac{k_0}{\|\bar{\boldsymbol{\alpha}}\|_{\text{NINT}}} \right\} \quad (4.27)$$

where the simplified discriminant, using Eq. (4.2), yields

$$D = \left(\bar{\mathbf{z}}:\mathbf{z} - \frac{2}{3}\bar{K}K\right)^2 - \left(\bar{\mathbf{z}}:\bar{\mathbf{z}} - \frac{2}{3}\bar{K}^2\right)\left(\mathbf{z}:\mathbf{z} - \frac{2}{3}K^2\right). \quad (4.28)$$

Each of the backstress components need to fulfill additional conditions when their depletion is imminent, as

$$\lambda_{\alpha_i} = \frac{\boldsymbol{\alpha}_i}{3\mathbf{n}_{\alpha_i}:\boldsymbol{\alpha}_i} \quad (4.29)$$

The limit plastic multiplier for the evolving distortion parameter is applicable for the second model only. As it has two mirrored asymptotic limits, the active one is chosen by the use of  $(\mathbf{n}_r:\mathbf{n}_z)$  as

$$\lambda_c = \min \left\{ \frac{c_2(\mathbf{n}_r:\mathbf{n}_z) - c}{3\bar{c}}; \frac{1}{\text{NINT}|\bar{c}|} \right\}. \quad (4.30)$$

## 4.2 Numerical tests

A novel approach accompanying the development of these models is the previously unseen focus on numerical testing from a wide range of perspectives. The value of virtually any internal variable can be meaningfully plotted and its changes observed in various scenarios, bringing new insight into the inner workings of the model or uncovering previously hidden inconsistencies.

### 4.2.1 Error maps

A helpful and well known way to test a model's implementation is an iso-error map. As the models in question produce error fields with much complexity, a contour plot would not be readable. Therefore, a combined plot presented in Fig. 4.5 includes an equi-strain map to give the reader better idea about the scale of the involved deformation. The error, defined by

$$\eta = \frac{\|\boldsymbol{\sigma} - \hat{\boldsymbol{\sigma}}\|}{k_0} \cdot 100 [\%], \quad (4.31)$$

is calculated by means of a 10 times finer subincrementation of the integration step. This particular map is important from several perspectives. First, with the setting of  $NINT = 50$ , the error reaches up to 2%, which is still manageable. Better precision is easily accessible via parameter  $NINT$ . However, a single, thin sliver at the very frontal apex reaches error of up to 20%. This is caused by fast behavior of Eq. 4.11 combined with low rate of plastic strain in tangential loading direction. This same behavior causes non-convex equi-strain lines within the first milistrain range, as the Yield Surface rotates fast around  $\beta$ .

Probably the most important notion is the preservation of high error even far away from the initial prestress (black circle). Contrary to simple models, where the error diminishes with the subsiding plastic modulus, in this model, the Bounding Surface continues to harden and maintains the acquired level of error. A map of the count of numerical steps is in Figure 4.6.

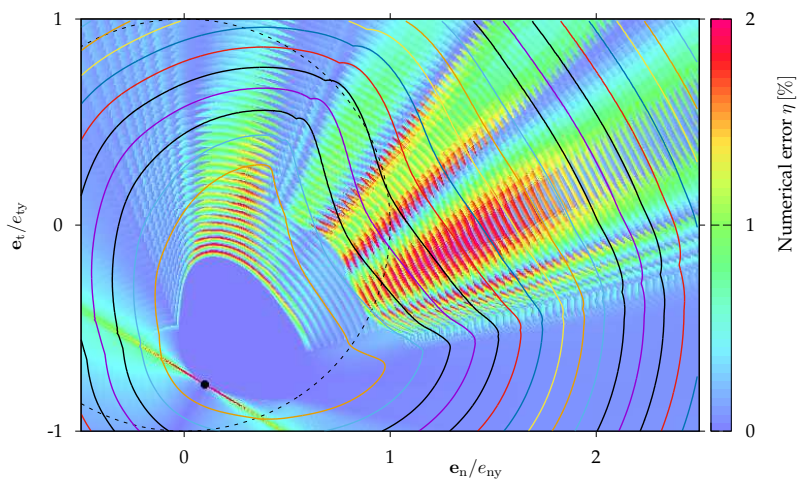


FIGURE 4.5: Combined plot of numerical error and plastic strain in deviatoric space.

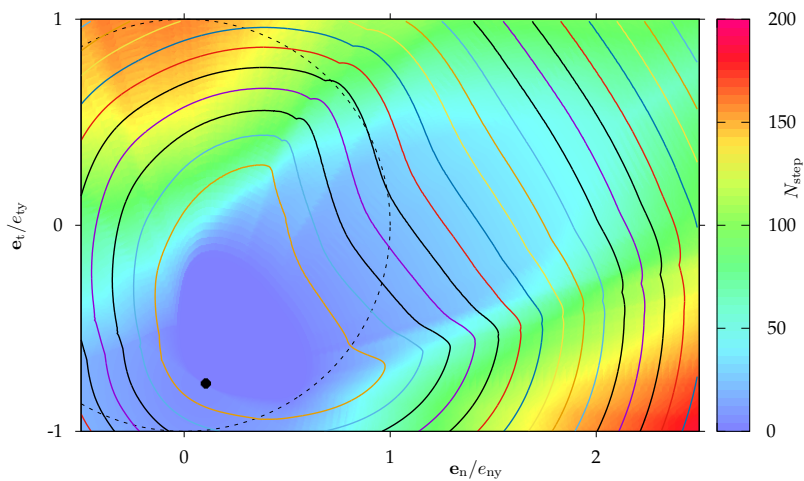


FIGURE 4.6: Combined plot of the number of integration steps and plastic strain in deviatoric space.

## Chapter 5

# Conclusion

Regarding the **theoretical outcomes of the thesis**, the two new models serve as a launching pad for research into low-cycle fatigue. Specific nature of experiments has been proposed to help tweak and calibrate these models for expected practical application, focusing on very small deformation in the scope of elasto-plastic transition, for which the internal evolution rules were intended. The simulation of springback is the next proposed step, however, the experimental investigation of sheet metal is much more difficult to master, especially considering the requirements of these particular models. The new experimental kinematic rule opens the possibility to model sequential distortion, the exact observed behavior of metal materials within the realm of very small deformation. Unifying the backstress components with the individual distortion directors would create a logically consistent model.

The **practical outcomes of the thesis** lie in the UMAT subroutines for Abaqus, making these models available to the community of engineers. Changing the evolution rules within the model is very easy, as it does not interfere with derivatives of the Yield Function. Preparing the model for particular practical application is now straight forward process, thanks to many tools developed during the work on this thesis, namely numerical calibration on a library of experiments and visualizing the internal state of the model, energy dissipation and other phenomena in tension-torsion as well as deviatoric stress plane.

From a multitude of tests it is evident that the act of proposing a new advanced model for multiaxial loading has to be accompanied by a deep study in its behavior. Analytical methods, used for testing some very specific conditions,

do help eliminate most of the encountered problems. Still, there are great many problems hiding in general application. To search for them, it is necessary to use brute-force approach in a large variety of tests.

The integration speed of the presented models is satisfactory. There are a number of possible ways of optimization. Using osculation hyperspheres for analytical solutions within a small angle at the apex of the surface could reduce the computational costs when calculating the plastic part of the trial stress as well as radial return stress correction. Using a midpoint rule for more precise evolution of internal variables is the most immediate proposition. Smooth positioning of the midpoint can eliminate discontinuities when the system chooses between first order Euler forward and a midpoint rule. Functions with extreme acceleration, like the hardening curve exhibiting smooth elastic-plastic transition, may have an optimal position of the midpoint to get the best precision.

Many unfounded decisions on the kinematic rule were made in the presented model. It is expected these models will continue to evolve when new information about the behavior of the material comes to light. The Institute of Thermomechanics of the CAS recently acquired means of advanced experimental testing, meeting the requirements of effective research into multiaxial ratcheting. One of many questions is whether counteracting and eliminating elongation due to distortion at the front apex is even practical.

## 5.1 Future ways of distortion generation

Unlike a continuous summation of distortions in [20], a sequence of discrete distortions has been recently studied. The new proposed yield function

$$f(\boldsymbol{\sigma}) = \sqrt{\frac{3}{2}} \|\mathbf{b}_N\| - k \quad (5.1)$$

employs the modified radial tensor  $\mathbf{b}^N$ . The initial radial tensor  $\mathbf{b}_0 = \mathbf{s} - \boldsymbol{\alpha}$  undergoes  $N$  successive transformations as

$$\mathbf{b}_{i+1} = \mathbf{b}_i + c_{i1} \mathbf{n}_{z_i} x_i \left[ \frac{1}{1 + c_{i2} x_i} + c_{i3} \right], \quad i = 0, 1, \dots, N - 1, \quad (5.2)$$

where  $x_i = \mathbf{n}_{zi} : \mathbf{b}_i$ . Each of the transformation is driven by unit-norm director  $\mathbf{n}_{zi}$ . Three evolved variables  $c_{1i}$ ,  $c_{2i}$  and  $c_{3i}$  for every single transformation control the axial distortion at the front and back as well as induced curvature of the frontal apex, see Figure 5.1.

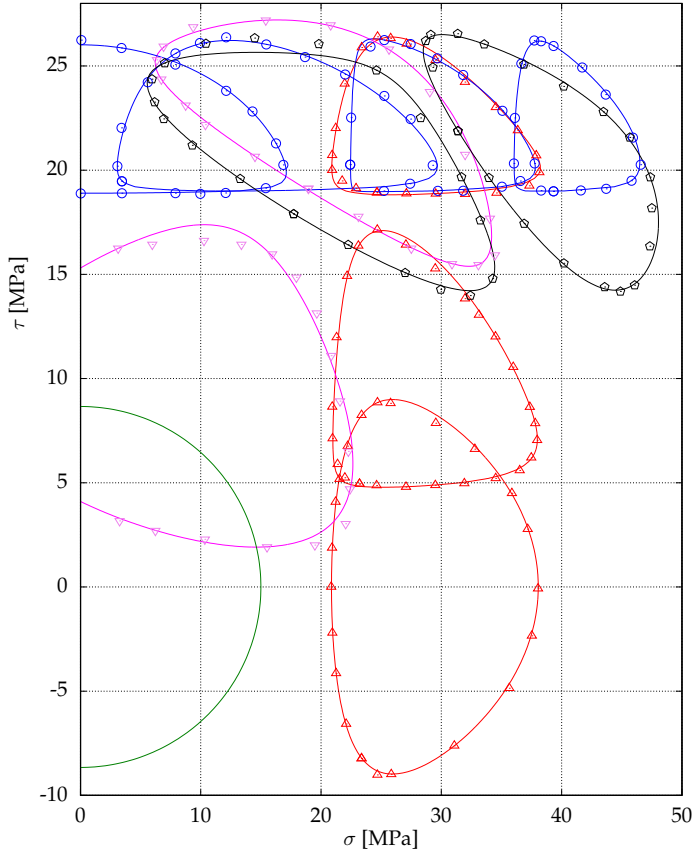


FIGURE 5.1: Demonstration of sequential multidirectional distortion.

The cross effect is controlled only by the isotropic parameter  $k$ . To demonstrate its capabilities, the yield function's internal variables have been calibrated to fit the previously mentioned series of measured yield surfaces. The distortion is induced by a hyperbolic function enabling high relative compression of the rear. Rather than choosing a two-value elongation of front and rear separately, this continuous function maintains first order continuity when applied on an arbitrary shape. Still, the results for more complex loading histories are uncertain. The combined distortion of non-orthogonal directors (black line on the right) was achieved by using incorrect choice of directors. To effectively solve this problem, much more data need to be measured. The main problem of this proposed model is the discrete series of directors needed for the distortion. Their movement, their introduction and disappearance has to be smooth, so that the stress response of such a model will be continuous. Only initial steps have been made to remedy this problem.

# Author's References

- [A1] MAREK, R., PLEŠEK, J., HRUBÝ, Z., PARMA, S., FEIGENBAUM, H., AND DAFALIAS, Y. Numerical implementation of a model with directional distortional hardening. *Journal of Engineering Mechanics* 141, 12 (2015), pp. 12–21.
- [A2] PARMA, S., PLEŠEK, J., MAREK, R., HRUBÝ, Z., FEIGENBAUM, H. P., AND DAFALIAS, Y. F. Calibration of a simple directional distortional hardening model for metal plasticity. *International Journal of Solids and Structures* 143 (2018), pp. 113–124.
- [A3] WELLING, C., MAREK, R., FEIGENBAUM, H., DAFALIAS, Y., PLEŠEK, J., HRUBÝ, Z., AND PARMA, S. Numerical convergence in simulations of multiaxial ratcheting with directional distortional hardening. *International Journal of Solids and Structures* (2017), pp. 105–121.

# Bibliography

- [1] CORONA, E., HASSAN, T., AND KYRIAKIDES, S. On the performance of kinematic hardening rules in predicting a class of biaxial ratcheting histories. *International Journal of Plasticity* 12, 1 (1996), pp. 117–145.
- [2] DAFALIAS, Y. F., AND POPOV, E. P. A model of nonlinearly hardening materials for complex loading. *Acta Mechanica* 21, 3 (1975), pp. 173–192.
- [3] FEIGENBAUM, H. P., AND DAFALIAS, Y. F. Simple model for directional distortional hardening in metal plasticity within thermodynamics. *Journal of Engineering Mechanics* 134, 9 (2008), pp. 730–738.
- [4] FEIGENBAUM, H. P., DUGDALE, J., DAFALIAS, Y. F., KOUROUSIS, K. I., AND PLESEK, J. Multiaxial ratcheting with advanced kinematic and directional distortional hardening rules. *International Journal of Solids and Structures* 49, 22 (2012), pp. 3063–3076.
- [5] FREUND, M., SHUTOV, A., AND IHLEMANN, J. Simulation of distortional hardening by generalizing a uniaxial model of finite strain viscoplasticity. *International Journal of Plasticity* 36 (2012), pp. 113–129.
- [6] HASSAN, T., CORONA, E., AND KYRIAKIDES, S. Ratcheting in cyclic plasticity, part ii: Multiaxial behavior. *International Journal of Plasticity* 8, 2 (1992), pp. 117–146.
- [7] HASSAN, T., AND KYRIAKIDES, S. Ratcheting in cyclic plasticity, part i: Uniaxial behavior. *International Journal of Plasticity* 8, 1 (1992), pp. 91–116.
- [8] KURTYKA, T., AND ŻYCZKOWSKI, M. A geometric description of distortional plastic hardening of deviatoric materials. *Archives of Mechanics* 37, 4–5 (1985), pp. 383–395.

- [9] KURTYKA, T., AND ŻYCZKOWSKI, M. Evolution equations for distortional plastic hardening. *International Journal of Plasticity* 12, 2 (1996), pp. 191–213.
- [10] MAHAN, M., DAFALIAS, Y. F., TAIEBAT, M., HEO, Y., AND KUNNATH, S. K. Sanisteel: Simple anisotropic steel plasticity model. *Journal of Structural Engineering* 137, 2 (2011), pp. 185–194.
- [11] MATTHIES, H., AND STRANG, G. The solution of nonlinear finite element equations. *International journal for numerical methods in engineering* 14, 11 (1979), pp. 1613–1626.
- [12] ORTIZ, M., AND POPOV, E. P. Distortional hardening rules for metal plasticity. *Journal of Engineering Mechanics* 109, 4 (1983), pp. 1042–1057.
- [13] ORTIZ, M., AND POPOV, E. P. Accuracy and stability of integration algorithms for elastoplastic constitutive relations. *International Journal for Numerical Methods in Engineering* 21, 9 (1985), pp. 1561–1576.
- [14] PLEŠEK, J., FEIGENBAUM, H. P., AND DAFALIAS, Y. F. Convexity of yield surface with directional distortional hardening rules. *Journal of Engineering Mechanics* 136, 4 (2010), pp. 477–484.
- [15] PLEŠEK, J., AND KŘÍSTEK, A. Assessments of methods for locating the point of initial yield. *Computer Methods in Applied Mechanics and Engineering* 141, 3–4 (1997), pp. 389–397.
- [16] ROKHGIREH, H., NAYEBI, A., AND CHABOCHE, J. Application of a new distortional yield surface model in cyclic uniaxial and multiaxial loading. *International Journal of Solids and Structures* 110–111 (2017), pp. 219–238.
- [17] SHUTOV, A. V., AND IHLEMANN, J. A viscoplasticity model with an enhanced control of the yield surface distortion. *International Journal of Plasticity* 39, 0 (2012), pp. 152–167.
- [18] SHUTOV, A. V., AND IHLEMANN, J. On the phenomenological modeling of yield surface distortion.

- [19] SLOAN, S. W. Substepping schemes for the numerical integration of elasto-plastic stress–strain relations. *International Journal for Numerical Methods in Engineering* 24, 5 (1987), pp. 893–911.
- [20] VOYIADJIS, G. Z., AND FOROOZESH, M. Anisotropic distortional yield model. *J. App. Mech.* 57, 3 (1990), pp. 537–547.
- [21] WILKINS, M. L. Calculation of elastic-plastic flow. *Methods of Computational Physics* 3, 0 (1964), pp. 389–397.
- [22] ZHANG, M., BENÍTEZ, J. M., AND MONTÁNS, F. J. Capturing yield surface evolution with a multilinear anisotropic kinematic hardening model. *International Journal of Solids and Structures* 81 (2016), pp. 329–336.